

CONVERGENCE AND STABILITY IN UPSCALING OF FLOW WITH INERTIA FROM PORESCALE TO MESOSCALE

MAIGORZATA PESZYŃSKA * AND ANNA TRYKOZKO †

Abstract. We propose an algorithm for computational upscaling of flow with inertia from porescale (microscale) to Darcy scale (lab scale, mesoscale). In particular, we solve Navier-Stokes equations in complex pore geometries and average their solutions to derive properties of flow relevant at lab scale in non-Darcy model of flow. Convergence and stability of the algorithm are discussed. The project is a prototype of a computational laboratory for porous media which delivers the data for non-Darcy model with inertia at mesoscale.

1. Introduction. In [1] we presented a proof-of-concept algorithm for computational upscaling from porescale (microscale) to Darcy scale (laboratory scale \equiv mesoscale)¹. Here we provide details and an in-depth study of that algorithm and in particular, are concerned with its convergence and stability.

Until recently, computational modeling of flow in porous media has been constrained to the scales of physical observation, i.e., to the Darcy scale. Beyond Darcy scale, coefficients for large scale flow simulations in aquifers and oil-gas reservoirs are obtained by upscaling from meso- to macroscale [2, 3, 4]. Recently, modeling of flow and transport phenomena at porescale has become feasible thanks to increases in computational power and development of discrete models such as network and lattice models. These efforts, accompanied by advances in micro-imaging of porescale, help to understand processes such as capillary effects at porescale and their implications at other scales [5, 6, 7, 8].

In this paper we are interested in quantitative description of inertia effects at microscale and mesoscale. Our project can be seen as a part of a computational laboratory for modeling flow with inertia in porous media over a range of scales; further upscaling to macroscale can follow, e.g., [9]. We consider i) continuum flow mod-

*Dept. of Math., Oregon State University, Corvallis, OR, 97331 (mpesz@math.oregonstate.edu)

†IM, University of Warsaw, Pawińskiego 5a, 02-106 Warszawa, Poland (A.Trykozko@icm.edu.pl)

¹We will use the names for these scales interchangeably in this paper

els, i.e., traditional discretizations of Navier–Stokes equations applicable at porescale, and ii) an upscaling algorithm from porescale to mesoscale. We investigate conditions under which the combination of i) and ii) can be used efficiently to deliver reliable quantitative information at mesoscale.

Specifically, at porescale, we consider stationary incompressible viscous flow in laminar flow regime, characterized by Reynolds number Re not exceeding 10. At mesoscale we use a nonlinear non-Darcy model.

The main difficulties of the project are the following. First, standard discretization techniques for Navier-Stokes equations are well studied but their use in complex geometries requires fine grids and is, in general, nontrivial. Second, calculating average quantities from computational data is only superficially straightforward since the stability of results with respect to grids and algorithms over a large range of Reynolds numbers must be ensured.

Following initial success reported in [1], we address convergence and stability of the proposed algorithms with respect to computational grids at porescale and mesoscale in general anisotropic geometries. To our knowledge, this is the first such result in the literature. Related work in [10, 11, 12, 13] addressed the qualitative character of inertia at porescale without deriving upscaled models.

The paper is outlined as follows. In Sections 2 and 3 we describe the relevant physical models and computational techniques including upscaling to a full tensor. In Section 4 we present results on convergence and stability, and we close with conclusions in Section 5.

2. Mathematical models. Let Ω be an open bounded domain occupied by porous medium and the fluid within. For simplicity we consider $\Omega \subset \mathbb{R}^2$; results for \mathbb{R}^3 will be reported elsewhere. We denote by $(\mathbf{q})_i, i = 1, 2$ the components of a vector $\mathbf{q} \in \mathbb{R}^2$; we also denote position by $\Omega \ni \mathbf{X} = (X_1, X_2) = X_1 \mathbf{e}_1 + X_2 \mathbf{e}_2$ or $\mathbf{X} = (x, y)$.

Let Ω_F be the part of Ω occupied by the fluid and denote the rock (solid) by Ω_R . Let $\Gamma = \partial\Omega_F \cap \partial\Omega_R$ be the rock–fluid interface, and divide the external boundary of flow $\partial\Omega_F \cap \partial\Omega$ into the inflow Γ_{in} and outflow Γ_{out} parts. Numerical solutions are denoted with subscript h (microscale) and H (mesoscale).

2.1. Flow at porescale. We consider an incompressible Newtonian fluid of velocity \mathbf{u} and pressure p flowing in Ω_F . The fluid's viscosity is denoted by μ and the density by ρ . The flow is driven primarily by external boundary conditions, such as in a lab core. We prescribe inflow velocity at Γ_{in} whose maximum is denoted by u_{in} and whose shape is parabolic between the walls. On Γ_{out} we impose a numerical outflow condition [14]. On internal boundaries Γ we impose the *no-slip* condition $\mathbf{u} = 0$.

Recall the definition of $Re = \frac{|\mathbf{u}|d}{\mu}$ where d is a characteristic length in the domain of the flow, e.g., width of a channel or the diameter of porous grains. In our computational experiments we use μ, ρ reflecting properties of water in standard conditions in a lab. The values of $d, |\mathbf{u}|, \rho, \mu$ are such that $Re < 10$; the magnitude of \mathbf{u} and hence of Re is associated with the values of u_{in} . We recall that for flow in porous media the linear laminar flow regime corresponds to $Re < 1$, the nonlinear regime is for $1 \leq Re < 10$, and that turbulence may occur for $Re \geq 10$ [15, 16]; however, turbulence rarely occurs in porous media. For simplicity in the presentation below we set $\rho \equiv 1$. See Appendix for data and units.

At microscale (porescale), for steady-state flow, in the absence of forces and mass source/sink terms, the momentum and mass conservation in Eulerian frame are expressed by Navier-Stokes equations and continuity equation [17]. After rescaling variables with ρ, μ , we have

$$(2.1) \quad \nabla \cdot \mathbf{u} = 0,$$

$$(2.2) \quad \mathbf{u} \cdot \nabla \mathbf{u} - \mu \Delta \mathbf{u} = -\nabla p.$$

An alternative formulation in terms of the vorticity vector $\omega = \nabla \times \mathbf{u}$ and the (scalar) stream function ψ defined by $\mathbf{u} = \nabla \times \psi$ and its use for computational upscaling was considered in [1].

For small Re , the nonlinear convective, i.e., inertia terms associated with $\mathbf{u} \cdot$ are dropped from (2.2) and we have the (linear) Stokes approximation $-\mu \Delta \mathbf{u} = -\nabla p$, which is a valid approximation when viscous effects dominate in the flow.

2.2. Flow at Darcy scale. At Darcy (lab/mesoscale) the boundaries between Ω_F and Ω_R are not recognized. Instead, one considers an average flow in Ω characterized by average pressure P and velocity (flux) \mathbf{U} . Mass conservation holds $\nabla \cdot \mathbf{U} = 0$. The flow in Ω is driven by boundary conditions which average external porescale boundary conditions.

Darcy's law is a linear momentum equation at mesoscale

$$(2.3) \quad \mathbf{K}^{-1}\mathbf{U} = -\nabla P,$$

where the values of a symmetric permeability tensor \mathbf{K}^2 are measured experimentally [16]. In general, $\mathbf{K} = \begin{bmatrix} K_{11} & K_{12} \\ K_{21} & K_{22} \end{bmatrix}$ and is symmetric; if the eigenvectors, i.e., principal directions $\mathbf{v}_1, \mathbf{v}_2$ of \mathbf{K} coincide with $\mathbf{e}_1, \mathbf{e}_2$, then \mathbf{K} is diagonal. Further, if $K_{11} = K_{22}$, the medium is isotropic. Due to large viscous dissipation and interstitial effects common in porous media, Darcy's law is a good approximation for a large class of flow phenomena. Note that the flow at Darcy scale is assumed irrotational while at porescale it is not [18].

For large flow rates, in the nonlinear laminar regime with significant inertia, non-Darcy model which extends (2.3) reads

$$(2.4) \quad \mathcal{K}^{-1}(\mathbf{U})\mathbf{U} = -\nabla P.$$

In 1D, the Forchheimer model $\mathcal{K}^{-1}(U) := K^{-1} + \beta|U|$ was first proposed in [19]; it was extended to multidimensional isotropic media [20, 16, 15, 21] and is used in petroleum industry around wells [22] in the form

$$(2.5) \quad \mathcal{K}^{-1}(\mathbf{U})\mathbf{U} := (\mathbf{K}^{-1} + \beta|\mathbf{U}|)\mathbf{U} = -\nabla P$$

The form of nonlinear map \mathcal{K} for general anisotropic 2D and 3D media has been the subject of theoretical research [23, 24, 25, 26, 27, 28]; there exist controversies and

²a different model including viscosity explicitly is $\mathbf{K}^{-1}\boldsymbol{\mu} = -\nabla P$

inconsistencies as concerns the form and measurements of \mathcal{K} .

2.3. Mathematical upscaling from micro- to mesoscale. In order to up-scale, i.e., to compute coefficients of a model at a higher scale, there are in general two methodologies that apply. The homogenization theory gives elegant theorems on convergence of the averages of microscale quantities to the appropriate mesoscale quantities when the size of periodic cell goes to 0, but it requires periodic geometry. The second, volume averaging, does not restrict geometry and proposes that the averaged quantities are reasonably stable if the averaging region (REV \equiv Representative Elementary Volume) is large enough. However, it may be difficult to quantify what size of REV is sufficient; see [29] for related work on elasticity. In this work we are motivated by work in [2] for porous media which does not require periodic geometry.

The idea to connect porescale and lab scale models for porous media flow is via averaging and identification $\mathbf{U} = \langle \mathbf{u} \rangle_V, P = \langle p \rangle_V$. (Here we define local average over a volume $V(\mathbf{X})$ centered at $\mathbf{X} \in \Omega$ as $\langle q \rangle_V \equiv \langle q \rangle(\mathbf{X}) \equiv \frac{1}{|V(\mathbf{X})|} \int_{V(\mathbf{X})} q(\mathbf{Y}) d\mathbf{Y}$.) This was first formalized by Tartar in [30] who connected the Stokes model to Darcy model (2.3) via homogenization theory [31, 32]; the values of \mathbf{K} computed by homogenization reflect the geometry of porescale Ω_F .

In the nonlinear laminar regime with significant inertia, the connection between Navier-Stokes equations at porescale (2.2) and non-Darcy model (2.4) was considered by many authors [23, 24, 26, 27, 33]; there exist controversies as concerns the mathematical form of (2.4).

In this paper we explore computational upscaling from porescale to lab scale, i.e., we use approximate solutions \mathbf{u}_h, p_h at porescale and their averages $\mathbf{U}_H \approx \langle \mathbf{u}_h \rangle_V, P_H \approx \langle p \rangle_V$ over volumes V of $|V| = O(H)$ in order to identify terms in a discrete counterpart of (2.5). In the process, we compute the coefficients \mathbf{K}, β parametrizing \mathcal{K} in (2.5).

3. Computational models. Here we briefly describe computational models for \mathbf{u}_h, p_h and \mathbf{U}_H, P_H and give details on the upscaling procedure.

3.1. Computational models for porescale. In this paper we use an algorithm solving Navier–Stokes equations for \mathbf{u}_h, p_h which can be used in complex pore geometries with fine grids; it is based on finite-volume discretization [34, 35, 14] on staggered grids. The implementation is under ANSYS FLUENT software which sets an industry standard in computational fluid dynamics [35, 34]; general unstructured grids can be used in 2D and 3D. The algorithm is convergent with rate $O(h)$ in both unknowns. See Section 4 for results.

We note that in [1] we considered additionally another algorithm in (ω_h, ψ_h) formulation which can be easily adapted to interpret data from porescale imaging [7] and is nicely enhanced by treatment of boundary conditions and post-processing. See also [14, 36] for other algorithms.

3.2. Computational model at Darcy scale. Our approach is to identify the averages of porescale solutions $\langle \mathbf{u}_h \rangle, \langle p_h \rangle$ with some discrete values \mathbf{U}_H, P_H at Darcy scale. Strictly speaking, we do not pursue any further computations at that scale; however, these may be considered as future elements of the computational laboratory.

Therefore, we choose a computational grid and discretization at mesoscale. Our approach is inspired by the conservative cell-centered finite difference (CCFD) method and it provides a bridge to macroscale following [9] in which non-Darcy flow was discretized for diagonal \mathbf{K} and \mathcal{K} . Low-order conservative methods have been very popular in computational models of subsurface for decades [37, 38]; the CCFD method is equivalent to lowest order Mixed Finite Element method on rectangles [38, 39]. CCFD is known to converge with order $O(H)$ in both the pressure and velocity variables; extensions to nonrectangular grids and superconvergence results for smooth solutions and grids are also known, see, e.g., [39] for more references.

Consider then a rectangular grid over Ω ; cell centers are associated with pressure unknowns P_H and cell edges are associated with degrees of freedom of (piecewise linear) velocity unknowns \mathbf{U}_H . The discretization of (2.3) depends on whether \mathbf{K} is a diagonal or a full tensor [39] and is associated, respectively, with a 5- or 9- point stencil in 2D (7- or 19- in 3D, respectively).

In this work we are interested in upscaling from microscale and do not need

to employ the 9–point stencil but rather follow some ideas from homogenization as applied to mesoscale upscaling in porous media in [2]. We describe them now.

3.3. Upscaling to find \mathbf{K} . Assume we know porescale geometry, i.e., Ω_F and Ω_R around some point $\mathbf{X}_0 \in \Omega$. Define a porescale grid over a Ω_F and solve for \mathbf{u}_h, p_h in a series of computational experiments $j = 1, 2, \dots$, with boundary conditions forcing the flow in various directions³, different for each j ; label the solutions corresponding to an experiment j by \mathbf{u}_h^j, p_h^j .

Next, superimpose over Ω a mesoscale rectangular grid composed of macrocells. Consider one such macrocell Ω_0 , making sure that the boundaries of Ω_0 are far enough from inlet and outlet boundaries $\Gamma_{in}, \Gamma_{out}$. Find P_H^j, \mathbf{U}_H^j on Ω_0 and $\mathbf{K}|_{\Omega_0}$ using the data P_H^j, \mathbf{U}_H^j and the algorithm below.

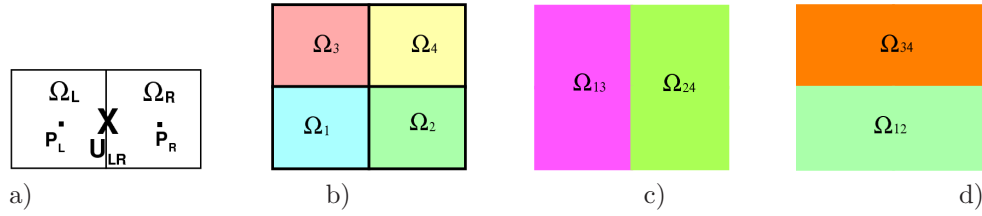


FIG. 3.1. Schematic figure of CCFD grid and macrocells used in upscaling. a) CCFD set-up for diagonal tensor, b) the region $\Omega_0 = \bigcup_{k=1}^4 \Omega_k$, and c) regions $\Omega_L \equiv \Omega_{13}, \Omega_R \equiv \Omega_{24}$ and d) $\Omega_T \equiv \Omega_{34}, \Omega_B \equiv \Omega_{12}$

3.3.1. Computing diagonal tensor \mathbf{K} . Assume first \mathbf{K} is diagonal and that the macrocell grid is aligned with its principal directions. Divide Ω_0 into a union of two cells $\Omega_0 = \Omega_L \cup \Omega_R := \Omega_{LR}$ as shown in Figure 3.1. For the flow aligned with \mathbf{e}_1 we have the discrete form of Darcy’s law (2.3)

$$(3.1) \quad U_{LR} := (\mathbf{U})_1 := (\langle \mathbf{u} \rangle_{\Omega_{LR}})_1 = K_{11} G_{LR} := K_{11} \frac{P_L - P_R}{x_R - x_L}.$$

An analogous equation $U_{BT} = K_{22} G_{BT}$ can be written if the flow direction is aligned with \mathbf{e}_2 and $\Omega_0 = \Omega_B \cup \Omega_T$.

The values of K_{11} and K_{22} must be computed from separate flow experiments with global flow direction \mathbf{U} aligned with \mathbf{e}_1 and \mathbf{e}_2 , respectively. In a way, this case

³In practice we find that using orthogonal directions of flow works best

is similar to using Dirichlet boundary conditions in [2].

3.3.2. Computing full tensor \mathbf{K} . Now consider a full tensor \mathbf{K} , i.e., the macrocell grid is not aligned with its principal directions. To determine \mathbf{K} , we follow loosely the ideas from [2]. We use an ansatz

$$(3.2) \quad P|_{\Omega_0} \approx P_0 + \nabla P \cdot (\mathbf{X} - \mathbf{X}_0).$$

To compute \mathbf{K} , we match $\mathbf{U} = \langle \mathbf{u} \rangle_{\Omega_0}$ to $\mathbf{K} \nabla P$. That is, we need ∇P .

In [2] the value ∇P is prescribed from boundary conditions; the periodicity is imposed on velocity and on almost all pressure unknowns. In our case, the flow is of Navier-Stokes type at porescale and this is not directly possible; instead, we design (computational) flow experiments so that ∇P is easy to find.

Now we divide the macrocell Ω_0 into four cells $\Omega_k, k = 1, \dots, 4$ arranged as in Figure 3.1. For each flow experiment j and cell k , we calculate $\mathbf{U}_k^j := \langle \mathbf{u}_h^j \rangle_{\Omega_k}$ and $P_k^j := \langle p_h^j \rangle_{\Omega_k}$.

Next we find, for each j , the linear approximation (3.2). We define $P_0^j := \langle p_h^j \rangle_{\Omega_0}$. To determine the components of the gradient ∇P^j , we combine the cell averages of \mathbf{u}_h^j, p_h^j according to the pattern $\Omega_L := \Omega_1 \cup \Omega_3, \Omega_R := \Omega_3 \cup \Omega_4, \Omega_B := \Omega_1 \cup \Omega_2, \Omega_T := \Omega_3 \cup \Omega_4$, see Figure 3.1 c) and d). We calculate $G_{LR} = \frac{P_L - P_R}{x_R - x_L}$ and $G_{BT} = \frac{P_B - P_T}{y_T - y_B}$ and now we can set $\nabla P^j|_{\Omega_0} := (G_{LR}^j, G_{BT}^j)$. The velocity is computed as $\mathbf{U}^j = \langle \mathbf{u}_h^j \rangle_{\Omega_0}$.

By matching $\mathbf{U}^j = -\mathbf{K} \nabla P^j$ we obtain (compare with (3.1))

$$(3.3) \quad \begin{cases} U_{LR}^j &= K_{11} G_{LR}^j + K_{12} G_{BT}^j \\ U_{BT}^j &= K_{21} G_{LR}^j + K_{22} G_{BT}^j \end{cases}, \quad j = 1, 2, \dots$$

Collecting the results for two experiments $j = 1, 2$ we have

$$(3.4) \quad \begin{bmatrix} U_{LR}^1 \\ U_{BT}^1 \\ U_{LR}^2 \\ U_{BT}^2 \end{bmatrix} = \begin{bmatrix} G_{LR}^1 & G_{BT}^1 & & \\ & & G_{LR}^1 & G_{BT}^1 \\ G_{LR}^2 & G_{BT}^2 & & \\ & & G_{LR}^2 & G_{BT}^2 \end{bmatrix} \begin{bmatrix} K_{11} \\ K_{12} \\ K_{21} \\ K_{22} \end{bmatrix}$$

This system is square; it is singular only if $G_{LR}^1 G_{BT}^2 = G_{LR}^2 G_{BT}^1$. This can only happen if the flow directions in experiments $j = 1, 2$ are parallel; by design we ensure that they are close to orthogonal. In the case when $U_{BT}^1 = 0, G_{BT}^1 = 0, U_{LR}^2 = 0, G_{LR}^2 = 0$, i.e., when flow directions are parallel to $\mathbf{e}_1, \mathbf{e}_2$, the system degenerates to the formulas in Section 3.3.1.

Note that we do not impose symmetry $K_{12} = K_{21}$ which is a fundamental property of the tensor \mathbf{K} . Rather, we verify whether \mathbf{K} is symmetric as a measure of quality of numerical experiments.

REMARK 3.1. *One can design more than two experiments and collect (3.3) for all $j = 1, 2, \dots$. However, an analogue of (3.4) will be overdetermined and a least-squares fit is necessary to calculate the entries of \mathbf{K} . Intuitively, more experiments would give more accurate information. Due to the presence of many small quantities, numerical instabilities lead however to inaccurate values of \mathbf{K} . In practice, (3.4) for two orthogonal experiments gives better results than a least-squares fit.*

The procedure described above allows us to find \mathbf{K} . Results in Section 4 show that \mathbf{K} remains essentially constant for a large range of flow rates. However, beginning at some u_{in} we observe the onset of the nonlinear regime, i.e., that \mathbf{K} or rather \mathcal{K} , start decreasing, as predicted by nonlinear non-Darcy model (2.4). In other words, the resistance \mathcal{K}^{-1} increases with increasing Re . This qualitative observation is fundamental and is consistent with one in upscaling from mesoscale to macroscale [9]. Below we discuss a quantitative model for \mathcal{K}^{-1} .

3.4. Upscaling porescale results to non-Darcy model. Above we showed how to compute \mathcal{K} for any Re . Now we fit the values of \mathcal{K} obtained for moderate Re to the non-Darcy flow model (2.5), i.e., we calculate the coefficients \mathbf{K} and β .

Since for small Re , the resistance \mathcal{K}^{-1} reduces to \mathbf{K}^{-1} as in (2.3), we set $\mathbf{K} = \mathcal{K}$ obtained for small u_{in} . Given \mathbf{K} and the values of \mathcal{K}, \mathbf{U} we find β by inverse modeling from (2.5). Clearly, if the model for \mathcal{K} is valid and the computational algorithm is successful, then the values of β should remain reasonably constant throughout the nonlinear laminar regime; this was confirmed first in [1].

With the methodology established, in the next section we are concerned with its

stability and convergence with respect to h , the size of REV (H), the choice of REV, and the principal values and axes of \mathbf{K} .

4. Results. Our expectations are that the combination of porescale computations and of upscaling delivers values of $\mathcal{K} \equiv \mathcal{K}(\mathbf{K}, \beta)$ which are stable and convergent with respect to h and H , regardless of the direction of porescale flow or mesoscale grids. Below we address these expectations.

The convergence of upscaled $\mathbf{K}_{h,H}$ which is a ratio of averages of p_h, \mathbf{U}_h over a region of size H should be considered in view of the following simple observations. Note that the averages $\langle p_h \rangle, \langle \mathbf{U}_h \rangle$ are linear quantities of interest [40] but the values of $\mathbf{K}_{h,H}$ are not. At the same time, as reported in [3] for upscaling from mesoscale to macroscale, the values of $\mathbf{K}_{h,H}$, for fixed H , appear to monotonically converge with h to the true values.

REMARK 4.1. *If a quantity q_h converges in $L_2(\Omega)$ norm to q with rate $O(h^\alpha)$, then its averages over a region Ω_0 converge to those of q at the same rate, with an additional multiplicative constant involving $\sqrt{|\Omega_0|} \approx O(\sqrt{H})$.*

LEMMA 4.1. *Let a_h, b_h be two real sequences convergent to a, b with rates α, β , respectively, as $h \rightarrow 0$, and let $|b_h| \geq b_0$ and $\min(b_0, |b|) > 0$. Then the quotient $\frac{a_h}{b_h}$ converges to $\frac{a}{b}$ with the rate at most $\min(\alpha, \beta)$.*

The lemma is established immediately from the inequalities

$$\begin{aligned} \left| \frac{a_h}{b_h} - \frac{a}{b} \right| &= \frac{|a_h b - ab + ab - ab_h|}{|b_h b|} \leq \frac{1}{|bb_h|} (|b||a_h - a| + |a||b - b_h|) \\ &\leq \frac{1}{b_0} \left(O(h^\alpha) + \frac{|a|}{|b|} O(h^\beta) \right). \end{aligned}$$

REMARK 4.2. *The rate of convergence of the quotient in Lemma 4.1 may not become apparent until h is sufficiently small. An instructive example is provided by $a_h = a + h; b_h = b - h^2$, for $a = 10^4, b = 10^{-4}$, where the rate $\alpha = 1$ is not observable until $h < 10^{-7}$. Since in porescale computations it may be impractical to use a very small h , one cannot, in general, expect for $\mathbf{K}_{h,H}$ to exhibit convergence rate. However, we expect it to be stable.*

Following Remarks 4.1, 4.2 we expect that $\langle \mathbf{u}_h \rangle_{\Omega_0}, \langle p_h \rangle_{\Omega_0}$ over a given region

$\Omega_0 \subseteq \Omega_F$ converge with rate $O(h)$. We expect furthermore that $G_{LR,h}$ and similar quantities converge with the same rate $O(h)$, but we do not know if $K_{h,H}$ will exhibit that rate. Note that all the mentioned quantities but $K_{h,H}$ are linear in \mathbf{u}_h, p_h .

We confirm the above expectations on some simple test cases reported below. In fact, we find that $\mathbf{K}_{h,H}$ appears to be stable with h and H and even to converge in synthetic porescale geometries. We also see that $\mathbf{K}_{h,H}$ appears to improve with increasing size of REV, i.e., H , which is consistent with ideas of REV but not with the estimate in Lemma 4.1.

4.1. Convergence of porescale computations with h . We set up computational experiments on geometries Ω_F with increasing complexity. Whenever practical, we use up to four levels of grid refinement. The regions $\Omega_0 \subset \Omega$ are always chosen away from inlet and outlet. Unless otherwise specified, we denote the error in the quantity $q \in \mathbb{R}$ by $E(q) := |q - q_h|$. If the value of q is not known, we estimate it by using the finest stable grid solution or by Richards extrapolation.

4.1.1. Poiseuille test case. This is a standard Poiseuille flow test case on $\Omega = (-D, D) \times (-1, 1)$ with $D=10$, and $\Omega_0 = (-1, 1)^2$. The analytical solution is $u_1(x, y) = (1 - y^2)Re$; $u_2(x, y) = 0$; $p(x, y) = (-2 * x + 2 * D)Re$. It is easy to compute the exact value of averages and of $K_{11} = 1/3$.

Table 4.1 presents the convergence results in pressure $E(p) := \|p - p_h\|_{L^2(\Omega_0)}$ and velocities $E(\mathbf{u}) := \|\mathbf{u} - \mathbf{u}_h\|_{L^2(\Omega_0)}$ as well as in some quantities used for upscaling; all appear to converge at the rate $O(h)$. \mathbf{K}_h computed as in Section 3.3.1 is stable but does not appear to converge monotonically.

4.1.2. Hourglass-shaped domain. This test case is similar to those performed in [11, 13]; geometry is shown in Figure 4.1, with ratio of radius to the width of the channel equal 0.7. This domain can be seen as a small cutout of the porescale geometry.

Table 4.2 shows results for $u_{in} = 1$. Here we do not know the analytical solution and do not attempt to estimate $E(\mathbf{u})$ or $E(p)$. Instead, we discuss convergence in the quantities of interest. Unfortunately, we do not observe $O(h)$ rate within the

	$E(\mathbf{u})$	$E(p)$	$E(\langle \mathbf{u} \rangle)$	$E(\langle p \rangle)$	$E(G_{LR})$	$K_{11,h}$
$Re = 1$						
ref. 1	0.1680	5.0312	0.0735	2.4997	0.2293	0.3350
ref. 2	0.0781	2.5259	0.0356	1.2626	0.1069	0.333
ref. 3	0.0378	1.3792	0.0171	0.6881	0.0517	0.3334
ref. 4	0.0192	0.6921	0.0084	0.3465	0.0199	0.3324
rate	1.0053	0.9120	1.0067	1.1992	1.1227	
$Re = 10$						
ref. 1	1.6803	50.5548	0.7348	25.1189	2.2811	0.33478
ref. 2	0.7808	26.1106	0.3565	13.0530	1.0686	0.3333
ref. 3	0.3779	14.9850	0.1711	7.47821	0.5164	0.3334
ref. 4	0.1934	8.23601	0.0843	4.12311	0.1916	0.3323
rate	1.0020	0.8339	1.0052	0.8310	1.1368	

TABLE 4.1

Convergence for Poiseuille case. Error is shown for various refinement levels *ref.1, ref.2, ...*. Also, the value of $K_{11,h}$ is shown.

considered range of values of h , and finer grids are impractical (see number of cells shown). We believe this is because this is a hard case of a converging-diverging flow with flow separation and vortices occurring at higher Reynolds numbers [13, 11, 12].

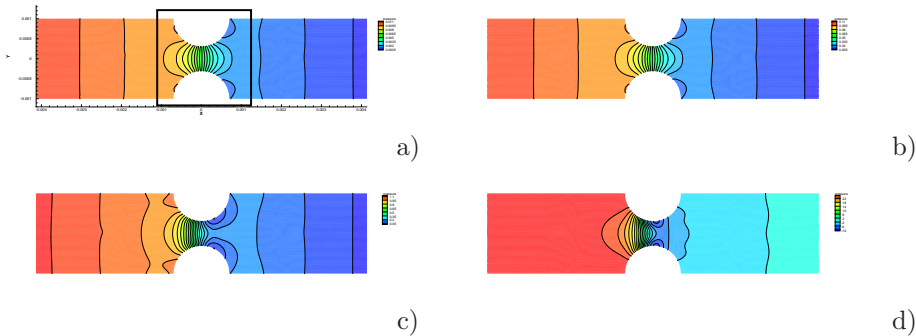


FIG. 4.1. Pressure profiles in the hourglass-shaped region, for $u_{in} =$ a) 10^{-4} , b) 10^{-3} , c) 10^{-2} , d) 10^{-1} obtained on the grid with third level refinement. Averaging region and dimensions are shown in a).

4.1.3. Synthetic porous medium. Now we consider a case similar to synthetic porous medium. Compared to the previous two cases, the geometry of Ω_F , see Figure 4.3, is quite complex. However, in a realistic porous medium, enough viscous dissipation occurs in the flow that the values of $\mathbf{K}_{h,H}$ behave smoothly and appear to converge in the given range of h , as shown below.

Results in this section concern an isotropic case in which the geometry of the

refinement level	1	2	3	4
$10^4 * h$	0.813998	0.4069991	0.2034996	0.1017498
number of cells	4090	16360	65440	261760
$G_{LR,h}$	41.312955	43.911519	53.967647	92.606832*
$U_{LR,h}$	0.001026193	0.00105264	0.001067912	0.0010748*
$10^4 * K_{11}$	0.24839	0.23972	0.19788	0.11606*

TABLE 4.2

Convergence of hourglass experiments: the quantities of interest appear monotone. The values marked with * appear iteration-unresolved

h	$u_{in} = 0.0001$	$u_{in} = 0.0005$	$u_{in} = 0.001$
0.000124859	4.30908e-006	4.30838e-006	4.30751e-006
6.24294e-005	3.86446e-006	3.86423e-006	3.86395e-006
3.12147e-005	3.75681e-006	3.75678e-006	3.75674e-006
1.40399e-005	3.72736e-006	3.72735e-006	3.72734e-006
rate	2.15199	2.15163	2.15129

TABLE 4.3

Values of $\mathbf{K}_{11,h}$ and convergence rate with h for a synthetic isotropic porous medium

porous grains is perfectly aligned with the directions of the flow; see Figure 4.3 (A). We can compute $\mathbf{K}_{h,H}$ using a special diagonal tensor algorithm from Section 3.3.1 or the general algorithm from Section 3.3.2. The latter delivers all values of $K_{11}, K_{12}, K_{21}, K_{22}$ which are shown in Table 4.2 and in Figure 4.2. We expect $K_{11} \approx K_{22}$ and that $K_{12} \approx K_{21} \approx 0$. This is confirmed in our results. Moreover, the results indicate monotone convergence of \mathbf{K}_h in h at a rate higher than expected.

In addition, comparing the values of \mathcal{K} for the geometry in Figure 4.3 A) with the one in B), as shown in Figure 4.2, we see that the latter ones are more stable. While it is somewhat *easier* in computational experiments to impose global flow over a synthetic domain to go from left to right or bottom to top, one actually obtains consistently better results with global flow patterns imposed at an angle to the principal directions of \mathbf{K} . This is likely caused by the relative lack of boundary layer formation when no “channels” from left to right (or bottom to top) can form.

4.2. Stability of anisotropic results and full tensor. Now we consider a synthetic porous medium in which the grains are ellipsoidal in shape with ratio of axes 9/6, see Figure 4.3(C). Moreover, we set-up an additional experiment, see Figure 4.3(D), in which the axes of the ellipses are at an angle of 30° to (x, y) ; a full

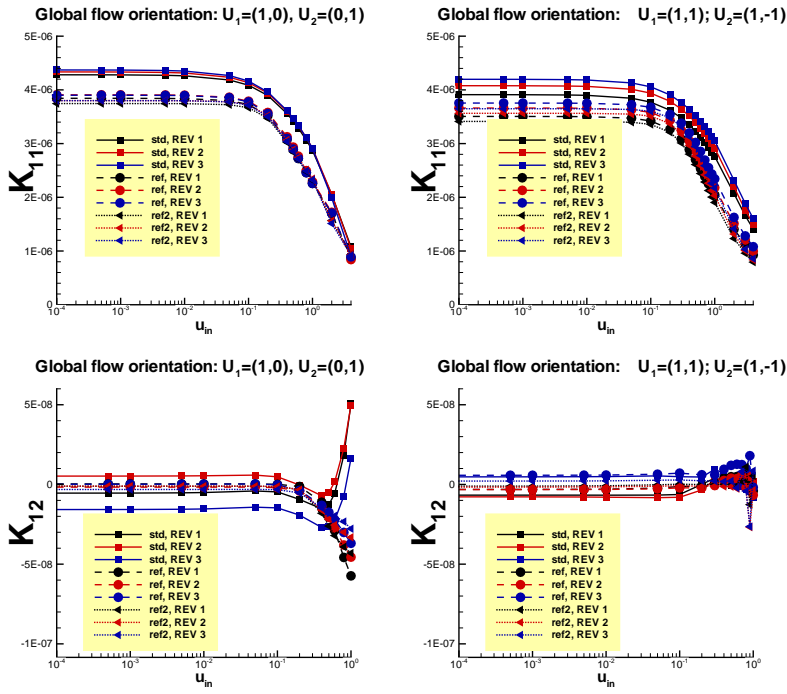


FIG. 4.2. Computational results for flow in (synthetic) porescale geometry. Shown are values of $\mathbf{K}_h \equiv \mathcal{K}_h$ depending on h and Re and on the flow direction as in Figure 4.3(A) and (B). Notice higher quality of results for $\mathbf{U}_1, \mathbf{U}_2$ not aligned with $\mathbf{v}_1, \mathbf{v}_2$.

tensor \mathbf{K} will be obtained in upscaling (D).

From the point of view of porescale calculations, there are no special challenges here as compared with the isotropic and/or diagonal case from Section 4.1.3. However, this test case verifies whether, fundamentally, our upscaling algorithm makes sense for general porous media in which \mathbf{K} and its principal directions are unknown a-priori and can change locally.

The flow and post-processing results are shown in Figure 4.4 for one value of h ; convergence is verified but won't be reported. We clearly see anisotropy in values of \mathbf{K} due to ellipsoidal shape of grains, resulting in a difference between K_{11} and K_{22} , as well as off-diagonal values of \mathbf{K} for case (D).

Additionally, we compute principal values and directions of the computed tensor \mathbf{K} for each of the inflow velocities. We find them at the expected angle 30° while the principal values for both cases essentially coincide, see Figure 4.4. Therefore, we conclude that our upscaling algorithm is sound.

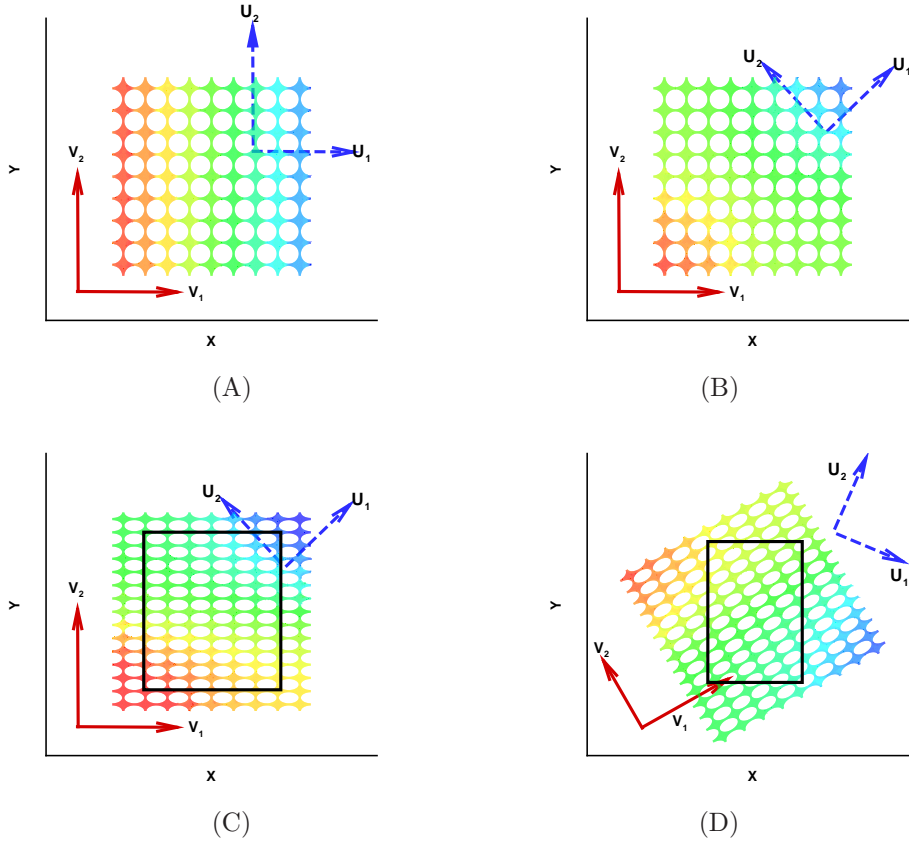


FIG. 4.3. Show are the pressure profiles as well as various directions involved in upscaling to diagonal and full tensor. \mathbf{K} is diagonal isotropic for (A) and (B), it is diagonal anisotropic for (C), and is a full tensor for (D). On all figures the direction of $\mathbf{e}_1, \mathbf{e}_2$ is denoted by the axes (x, y) . The principal directions of the tensor \mathbf{K} are denoted by $\mathbf{v}_1, \mathbf{v}_2$, and $\mathbf{U}_1, \mathbf{U}_2$ denote the global directions of flow, also visible from pressure profiles. The computed values of \mathbf{K} must be independent of $\mathbf{U}_1, \mathbf{U}_2$. In addition, principal values of \mathbf{K} should be independent of the direction of $\mathbf{v}_1, \mathbf{v}_2$ for the same geometry. The averaging region Ω_0 is shown in (C) and (D).

4.3. Convergence and stability with REV size H . Intuitively, averaging results of porescale computations should deliver better, i.e., more stable results for larger H . This is confirmed by results shown in Figure 4.4.

We see that the values of $\mathbf{K}_{h,H}$ decrease with increasing REV size; based on the similar monotone decreasing behavior with grid size h , this observation suggests that the values ‘improve’ with larger REV, as expected. Some anomalies arise for the largest REV where the boundary layer effects apparently play a role.

While logical, these results are at odds with the estimate in Lemma 4.1 which indicates that the values of $\mathbf{K}_{h,H}$ converge faster to the true value of \mathbf{K} with smaller

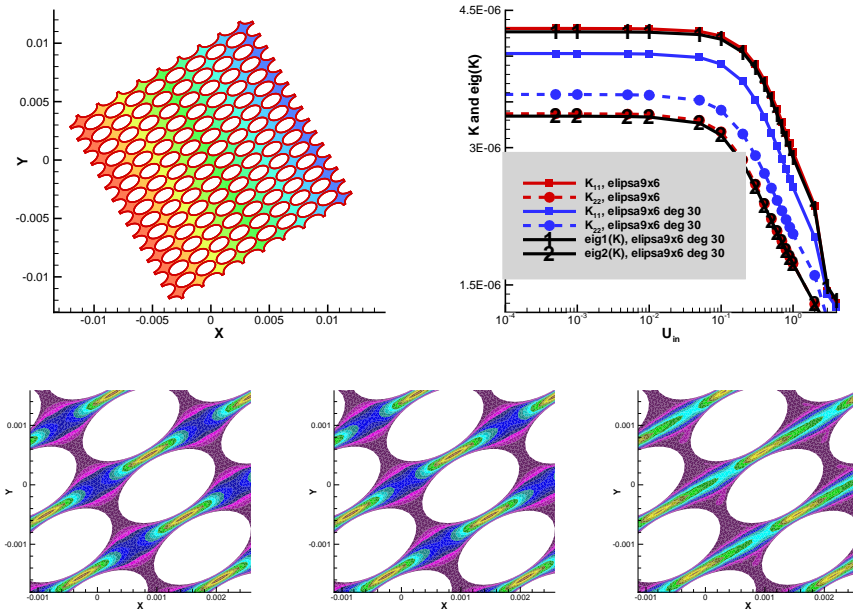


FIG. 4.4. Results of simulations for anisotropic geometry. A) Grid and pressure and (B) Upscaled values of \mathbf{K} . The (zoomed-in) profiles of velocity $(\mathbf{u}_h)_1$ with C) $u_{in} = .001$, D) $u_{in} = 0.1$ and E) $u_{in} = 1$ show changes in qualitative behavior for increasing flow rates.

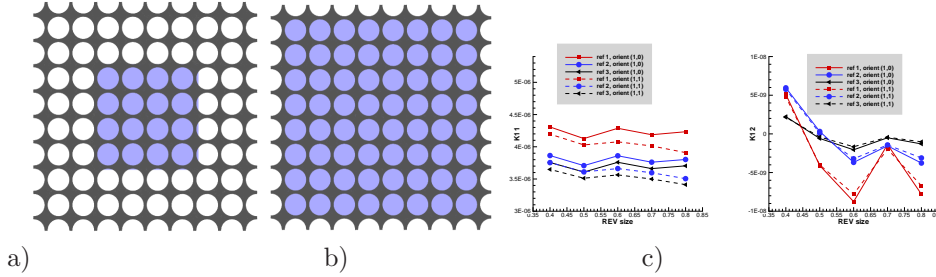


FIG. 4.5. Dependence of $K_{h,H}$ on REV size H . a) averaging regions for $REV3 \equiv H = 0.4$ and b) $REV1 \equiv H = 0.8$. c) Plot of $K_{11,h,H}$ and d) $K_{12,h,H}$ with respect to H .

H . We believe that the sample of REV sizes used in our computations is too small to adress this issue; we will take it up in future work.

4.4. Stability of inertia model and coefficients. The last step is to determine whether the quadratic inertia model (2.4) fits well the values of \mathcal{K} obtained for the case in Section 4.1.3. To this aim, we attempt to fit, in the inertia model from (2.5), the values of $\mathcal{K}^{-1} - \mathbf{K}^{-1}$ to $|\mathbf{U}|^\alpha$. If the Forchheimer model is valid, we should find that $\alpha \approx 1$ and a reasonably stable β .

ref. level	diagonal model				full velocity model			
	orient.=(1,0)		orient.=(1,1)		orient.=(1,0)		orient.=(1,1)	
	$10^{-6} * \beta$	α	$10^{-6} * \beta$	α	$10^{-6} * \beta$	α	$10^{-6} * \beta$	α
1	0.866	0.9836	1.05	0.996	0.618	0.984	0.748	0.995
2	1.18	1.145	1.51	1.167	0.834	1.14	1.06	1.16
3	1.61	1.387	1.83	1.406	1.14	1.38	1.28	1.41

TABLE 4.4

Results of fitting the upscaled resistance values \mathcal{K}^{-1} to $\mathbf{K}^{-1} + \beta|\mathbf{U}|^\alpha$ in Forchheimer model (2.5). We find that $\alpha \approx 1$ for coarse grids and that the values of β computed as a fit with $\alpha = 1$ are reasonably stable. In addition, we show the fit in the diagonal model in which $|\mathbf{U}|$ is replaced by $|U_1|$.

We show the values of α, β in Table 4.4. The results show that the fit is not linear when \mathbf{u}_h, p_h are resolved on a fine grid. However, it is close to linear for coarse grids and a smaller range of flow rates (not reported).

We conclude that more studies are needed here, and we leave this and a discussion of appropriate anisotropic inertia model for future considerations.

5. Conclusions. In this paper, following [1], we proposed an algorithm which carries fluid flow information from porescale to mesoscale in linear and nonlinear laminar flow regimes. The algorithm delivers stable values of coefficients of Darcy and non-Darcy models at mesoscale. Convergence is apparent for some quantities, already within the range of grids used. In conclusion, our computational laboratory delivers useful coefficients at Darcy scale.

However, we found that more work is needed to identify the appropriate inertia model at Darcy scale especially in anisotropic geometries; this observation is not disjoint from controversies that exist about that model. In addition, for the model to become part of an “on-demand” computational laboratory, it has to deliver, e.g., the values of \mathbf{K}, β in a few minutes. Currently, the computational complexity is as follows. A set of $j = 1, 2$ experiments for geometry as in, e.g., Section 4.1.3 for 25 distinct values of u_{in} takes about 30 min. on 4 processors for grid refinement level 1, about 1h for level 2, and so on. Pre-processing and post-processing (grids, file transfer, averaging etc.) each take about twice as long per set. We hope that simpler models such as one in [1] as well as adaptivity can help to reduce the computational time.

Our current work [41] includes further analysis of non-Darcy models for anisotropic media as well as an adaptive connection to computations at mesoscale and macroscale.

Acknowledgements: The work of Peszynska was partially supported from NSF grant 0511190 and DOE grant 98089. We used computational facilities at ICM (Sun Constellation System with AMD Quad-Core Opteron 835X processors) as well as the facilities at Oregon State University including the COE cluster.

Appendix. Here we briefly provide values of coefficients used in simulations. We used $\rho = 998.2[kg/m^3]$, $\mu = 0/001003[Pa.s]$.

For the example from Section 4.1.3 we used $d = 0.0018[m]$ (diameter of grains of radius $0.9[mm]$). As a result we have $Re = 1791.386u_{in}$ when u_{in} is given in $[m/s]$. For example, $u_{in} = 0.001 \rightsquigarrow Re = 1.79$. For the example from Section 4.2 we used $d = 1.2[mm]$ (smaller axis of ellipsoidal grains) which gives, for $u_{in} = 0.001 \rightsquigarrow Re = 1.19$. For the hourglass example from Section 4.1.2 we used $d = 1.4[mm]$ (grain diameter) which gives, for $u_{in} = 0.001 \rightsquigarrow Re = 1.393$.

REFERENCES

- [1] Malgorzata Peszynska, Anna Trykozko, and Kyle Augustson. Computational upscaling of inertia effects from porescale to mesoscale. In G. Allen, J. Nabrzyski, E. Seidel, D. van Albada, J. Dongarra, and P. Sloot, editors, *ICCS 2009 Proceedings, LNCS 5544, Part I*, pages 695–704, Berlin-Heidelberg, 2009. Springer-Verlag.
- [2] L. J. Durlofsky. Numerical calculation of equivalent grid block permeability tensors for heterogeneous porous media. *Water Resources Research*, 27(5):699–708, 1991.
- [3] W. Zijl and A. Trykozko. Numerical homogenization of the absolute permeability using the conformal-nodal and mixed-hybrid finite element method. *Transp. Porous Media*, 44(1):33–62, 2001.
- [4] Y. Chen, L. J. Durlofsky, M. Gerritsen, and X. H. Wen. A coupled local global upscaling approach for simulating flow in highly heterogeneous formations. *Adv. Water Resour.*, 26:1041–1060, 2003.
- [5] M.G. Schaap, M.L. Porter, B.S.B. Christensen, and D. Wildenschild. Comparison of pressure-saturation characteristics derived from computed tomography and lattice boltzmann simulations. *Water Resour. Res.*, 43(W12S06), 2007.
- [6] C. Pan, M. Hilpert, and C.T. Miller. Pore-scale modeling of saturated permeabilities in random sphere packings. *Physical Review E.*, 64(066702), 2001.

- [7] W. Brent Lindquist. Network flow model studies and 3D pore structure. In *Fluid flow and transport in porous media: mathematical and numerical treatment (South Hadley, MA, 2001)*, volume 295 of *Contemp. Math.*, pages 355–366. Amer. Math. Soc., Providence, RI, 2002.
- [8] Sauro Succi. *The lattice Boltzmann equation for fluid dynamics and beyond*. Numerical Mathematics and Scientific Computation. The Clarendon Press Oxford University Press, New York, 2001. Oxford Science Publications.
- [9] C.R. Garibotti and M. Peszyńska. Upscaling non-Darcy flow. *Transport in Porous Media*, 80:401–430, 2009. published online March 13.
- [10] J. S. Andrade, U. M. S. Costa, M. P. Almeida, H. A. Makse, and H. E. Stanley. Inertial effects on fluid flow through disordered porous media. *Phys. Rev. Lett.*, 82(26):5249–5252, 1999.
- [11] K. J. Cho, M.-U. Kim, and H.D. Shin. Linear stability of two-dimensional steady flow in wavy-walled channels. *Fluid Dynamics Research*, 23:349–370, 1998.
- [12] S. Mahmud, A.K.M. Sadrul Islam, and M. A. H. Mamun. Separation characteristics of fluid flow inside two parallel plates with wavy surface. *Int. Journal of Eng. Sci.*, 40, 2002.
- [13] O. Coulaud, P. Morel, and J.P. Caltagirone. Numerical modelling of nonlinear effects in laminar flow through a porous medium. *J. Fluid. Mech.*, 190:393–407, 1988.
- [14] Pieter Wesseling. *Principles of computational fluid dynamics*, volume 29 of *Springer Series in Computational Mathematics*. Springer-Verlag, Berlin, 2001.
- [15] Adrian E. Scheidegger. *The physics of flow through porous media*. Revised edition. The Macmillan Co., New York, 1960.
- [16] Jacob Bear. *Dynamics of Fluids in Porous Media*. Dover, New York, 1972.
- [17] G. K. Batchelor. *An introduction to fluid dynamics*. Cambridge Mathematical Library. Cambridge University Press, Cambridge, paperback edition, 1999.
- [18] S. Irmay. On theoretical derivation of Darcy and Forchheimer fomulas. *A.G.U. Trans.*, 39, 1958.
- [19] P. Forchheimer. Wasserbewegung durch Boden. *Zeit. Ver. Deut. Ing.*, (45):1781–1788, 1901.
- [20] S. Ergun. Fluid flow through packed columns. *Chemical Engineering Progress*, 48:89–94, 1952.
- [21] F.L. Dullien. *Porous media*. Academic Press San Diego, 1979.
- [22] R. E. Ewing, R. D. Lazarov, S. L. Lyons, D. V. Papavassiliou, J. Pasciak, and G. Qin. Numerical well model for non-darcy flow through isotropic porous media. *Comput. Geosci.*, 3(3-4):185–204, 1999.
- [23] C. C. Mei and J.-L. Auriault. The effect of weak inertia on flow through a porous medium. *J. Fluid Mech.*, 222:647–663, 1991.
- [24] M. Fourar, R. Lenormand, M. Karimi-Fard, and R. Horne. Inertia effects in high-rate flow through heterogeneous porous media. *Transport in Porous Media*, 60:353–370(18), 2005.
- [25] H. Huang and J. Ayoub. Applicability of the Forchheimer equation for non-Darcy flow in porous media. *SPE Journal*, (SPE 102715):112–122, March 2008.

- [26] Tiziana Giorgi. Derivation of Forchheimer law via matched asymptotic expansions. *Transport in Porous Media*, 29:191–206, 1997.
- [27] Zhangxin Chen, Stephen L. Lyons, and Guan Qin. Derivation of the Forchheimer law via homogenization. *Transp. Porous Media*, 44(2):325–335, 2001.
- [28] W. Sobieski and A. Trykozko. Darcy and Forchheimer laws in experimental and simulation studies of flow through porous media. in review.
- [29] Nicolas Moës, J. Tinsley Oden, Kumar Vemaganti, and Jean-François Remacle. Simplified methods and a posteriori error estimation for the homogenization of representative volume elements (RVE). *Comput. Methods Appl. Mech. Engrg.*, 176(1-4):265–278, 1999.
- [30] Luc Tartar. Incompressible fluid flow in a porous medium—convergence of the homogenization process. In *Nonhomogeneous media and vibration theory*, volume 127 of *Lecture Notes in Physics*, pages 368–377. Springer-Verlag, Berlin, 1980.
- [31] Alain Bensoussan, Jacques-Louis Lions, and George Papanicolaou. *Asymptotic analysis for periodic structures*, volume 5 of *Studies in Mathematics and its Applications*. North-Holland Publishing Co., Amsterdam, 1978.
- [32] Enrique Sánchez-Palencia. *Nonhomogeneous media and vibration theory*, volume 127 of *Lecture Notes in Physics*. Springer-Verlag, Berlin, 1980.
- [33] Alain Bourgeat, Eduard Marusić-Paloka, and Andro Mikelić. Weak nonlinear corrections for Darcy’s law. *Math. Models Methods Appl. Sci.*, 6(8):1143–1155, 1996.
- [34] Fluent Inc. *Fluent User’s Guide, ver. 6.3*, 2006.
- [35] S. V. Patankar. *Numerical Heat Transfer and Fluid Flow FLUENT software*. (Hemisphere, Washington DC, 1980.
- [36] Howard C. Elman, David J. Silvester, and Andrew J. Wathen. *Finite elements and fast iterative solvers: with applications in incompressible fluid dynamics*. Numerical Mathematics and Scientific Computation. Oxford University Press, New York, 2005.
- [37] D. W. Peaceman. *Fundamentals of numerical reservoir simulation*. Elsevier Scientific Publishing Company, Amsterdam-Oxford-New York, first edition, 1977.
- [38] T. F. Russell and M. F. Wheeler. Finite element and finite difference methods for continuous flows in porous media. In R. E. Ewing, editor, *The Mathematics of Reservoir Simulation*, pages 35–106. SIAM, Philadelphia, 1983.
- [39] T. Arbogast, M. F. Wheeler, and I. Yotov. Mixed finite elements for elliptic problems with tensor coefficients as cell-centered finite differences. *SIAM J. Numer. Anal.*, 34(2):828–852, 1997.
- [40] Mark Ainsworth and J. Tinsley Oden. A posteriori error estimation in finite element analysis. *Comput. Methods Appl. Mech. Engrg.*, 142(1-2):1–88, 1997.
- [41] M. Peszyńska, A. Trykozko, and K. Kennedy. Sensitivity to anisotropy in non-Darcy flow model from porescale through mesoscale. submitted, 2010.